We are IntechOpen, the world's leading publisher of Open Access books Built by scientists, for scientists

6,900
Open access books available

185,000
International authors and editors

200M
Downloads

Our authors are among the

154
Countries delivered to

TOP 1%
most cited scientists

12.2%
Contributors from top 500 universities



WEB OF SCIENCE™

Selection of our books indexed in the Book Citation Index in Web of Science™ Core Collection (BKCI)

Interested in publishing with us?
Contact book.department@intechopen.com

Numbers displayed above are based on latest data collected.
For more information visit www.intechopen.com



Chapter

Crystallography of Precipitates in Metals and Alloys: (2) Impact of Crystallography on Precipitation Hardening

Yoshitaka Matsukawa

Abstract

Following the previous chapter, this chapter describes crystallography of second-phase precipitate particles in metals and alloys; the focus of this chapter is placed on the effect of crystallography of precipitates on precipitation hardening. Unlike nonmetallic composite materials whose strength is determined by the volume fraction ratio of constituent phases, the strength of metals and alloys can be several times greater by introducing a minor amount of precipitate particles such as 2%. The magnitude of strengthening (hardening) due to precipitates is, in traditional understanding, controlled by the shear modulus, whether or not the precipitates are harder than the matrix. The most recent major update in this research field is a discovery that crystallography of precipitates is another factor controlling the magnitude of strengthening. In the case where the slip plane of dislocations in precipitates is not parallel to that in the matrix, dislocations gliding in the matrix are unable to cut through the precipitates, resulting in intense hardening regardless of the shear modulus. This chapter also reviews the classical theory of precipitation hardening established in the 1950s–1960s, in order to sort out open questions to be resolved.

Keywords: precipitates, nucleation, crystal structure, strength, dislocations

1. Introduction

This chapter is a supplement to the previous chapter on crystallography of precipitate particles in metals and alloys, for the purpose of describing how the crystallography of precipitates practically affects the physical properties of entire the material. The crystallography of precipitates is of interest not only for fundamental materials science but also for engineering, in particular, structural materials engineering. The strength of metals and alloys is highly affected by a minor amount of precipitates such as a few percent. In the case of nonmetallic composite materials, their strength is determined by the volume fraction ratio of constituent phases. In other words, the strength of nonmetallic composites is expected not to exceed that of constituent phases. On the other hand, metals and alloys containing second-phase precipitate particles, say, 2% in volume fraction, can exhibit a strength several times greater than the matrix phase (**Figures 1–3**). Such intense hardening is

IntechOpen

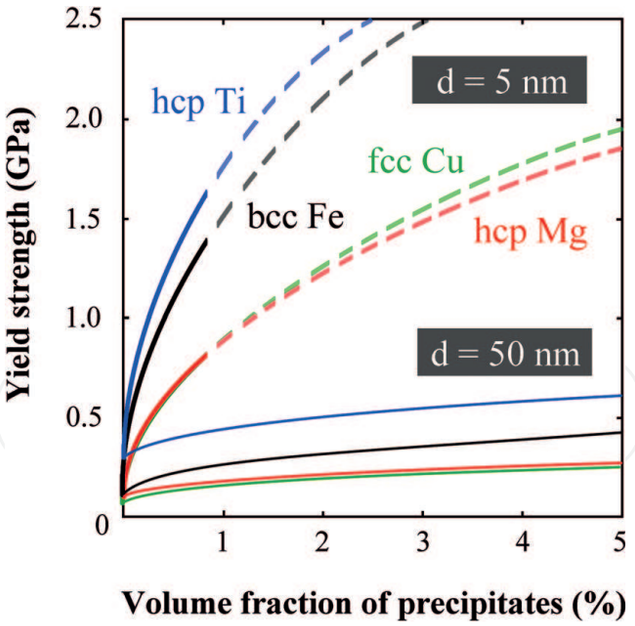


Figure 1.
A model calculation of precipitation hardening in the hcp Ti, the hcp Mg, the fcc Cu, and the bcc Fe, as a function of the volume fraction of precipitates for the cases of precipitate diameter of 5 and 50 nm. The obstacle strength is set to α = 0.8.

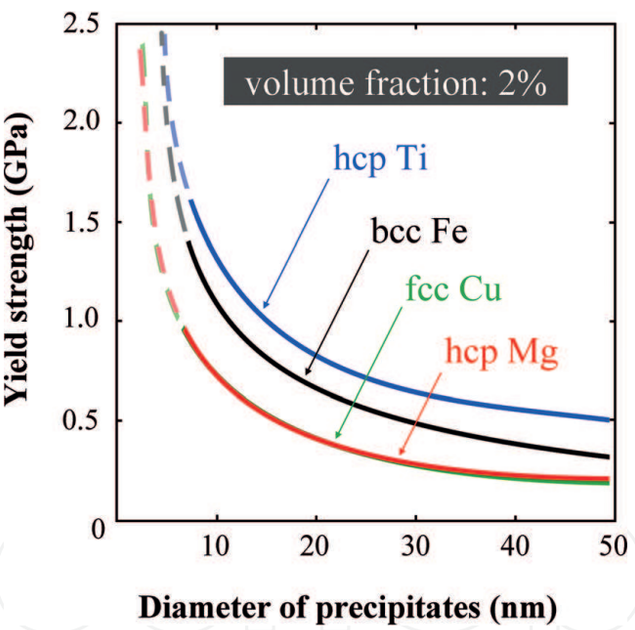


Figure 2.
A model calculation of precipitation hardening in the hcp Ti, the hcp Mg, the fcc Cu, and the bcc Fe, as a function of the diameter of precipitates for the case of precipitate volume fraction of 2%. The obstacle strength is set to α = 0.8.

achieved when precipitate particles are strong obstacles against the motion of dislocations gliding on a slip plane in the matrix. They are strong obstacles in the case where dislocations are unable to cut through them (**Figure 4**). In the classical theory of precipitation hardening (a.k.a. dispersion strengthening) established in the 1950s–1960s, the obstacle strength is assumed to be determined by the shear modulus [1, 2]; those which are harder than the matrix are strong obstacles. In general, this condition is fulfilled by a combination of metallic matrix and nonmetallic compound precipitates such as oxides and carbides whose strength is typically a few GPa, which is ~10 times greater than the yield strength of metals. Recent experimental studies demonstrated that crystallography of precipitate particles is

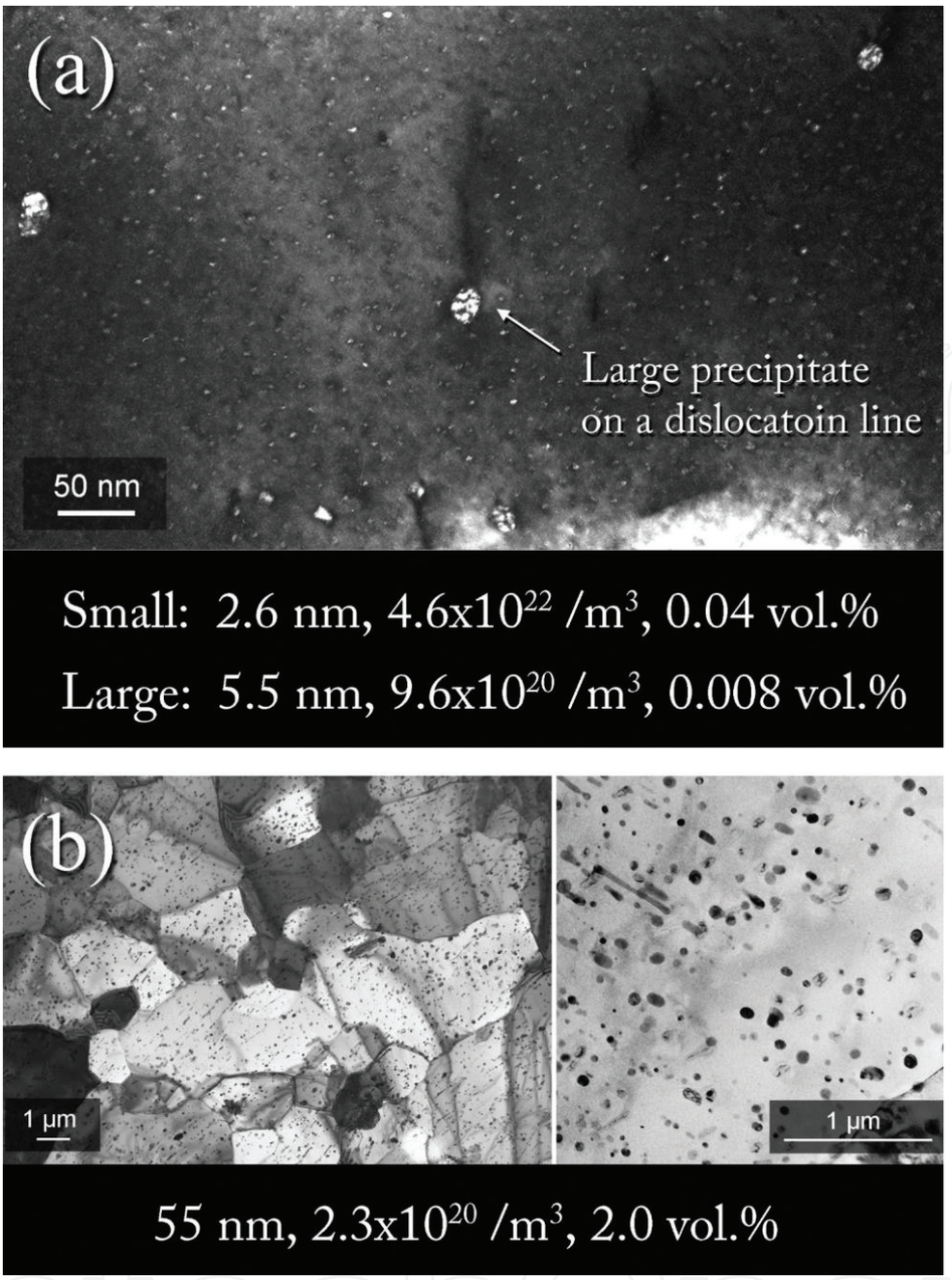


Figure 3.
Example of precipitate particles in alloys: (a) G-phase precipitates in a duplex stainless steel and (b) bcc Nb precipitates in a Zr—2.5Nb alloy [4].

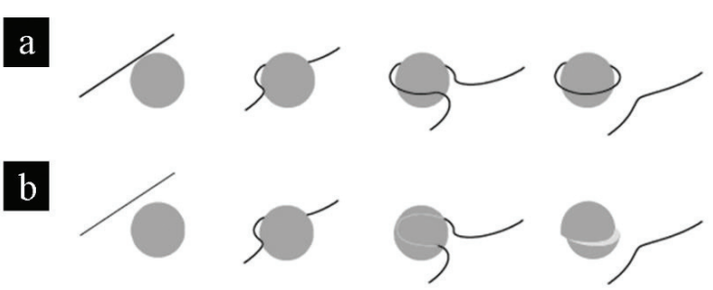


Figure 4.
Interaction between a gliding dislocation and a precipitate particle: (a) the Orowan mechanism for strong obstacles and (b) the cutting mechanism for weak obstacles [1]. The factor controlling the obstacle strength has been assumed to be the shear modulus, i.e., precipitates harder than matrix are strong obstacles. This concept has recently been updated; crystallography of precipitates is another factor controlling their obstacle strength.

another factor dominating their obstacle strength [3, 4]. When the slip plane in precipitates is not parallel to that in the matrix, dislocations gliding in the matrix are unable to cut through the precipitates regardless of the shear modulus. In this case, metallic precipitates are strong obstacles as well as nonmetallic compound precipitates. It follows that metals and alloys can be several times stronger than their constituent phases. In this way, crystallography enables us to create strong materials from a combination of weak materials: one plus one becomes more than two.

2. Magnitude of hardening as a function of precipitate size and number density

The abovementioned statement about the magnitude of precipitation hardening of the case of 2% volume fraction is derived from the following numerical calculation. Based on a geometry consideration of dislocation-precipitate interaction, the increase of material's yield strength, σ_y, which is a critical stress level where the deformation mode changes from elastic to plastic deformation, is given as follows [3, 5–7]:

$$\Delta\sigma_y = \alpha M \mu b (N_v d)^{1/2} \tag{1}$$

where α is the obstacle strength of the precipitates, M is the Taylor factor, μ is the shear modulus of the matrix, b is the magnitude of the Burgers vector of dislocations in the matrix, and N_v and d are the number of precipitate particles per unit volume (i.e., the number density) and their mean diameter. The Taylor factor (M) is a material-specific constant primarily dependent on the crystal structure, slip systems, and texture. An M value of 3.1 is commonly applied to non-textured polycrystalline metals having an fcc structure or a bcc structure [5–7]. For metals having an hcp structure, M values of 6.5 and 5.0 are commonly applied to Mg [8, 9] and Ti [10, 11], respectively. Their difference is related to the number of active slip system, which is dependent on the c/a ratio. The c/a ratio is 1.633 for ideal close-packed structure, 1.623 for Mg, and 1.587 for Ti. In the hcp Mg only the basal plane is available for dislocation slip, whereas in the hcp Ti, the primary slip plane is the prism plane, and the basal plane is also available as a secondary slip plane. In the traditional concept of the Orowan hardening, the obstacle strength (α) is dependent on the shear modulus. The obstacle strength of strong obstacles is, in theory, α = 1. However, when particles are dispersed in random distribution, the obstacle strength α is no longer 1, but instead a factor of 0.80–0.85 is introduced [12–16].

In the past several years, Eq. (1) has been frequently cited especially in the research community of nuclear materials, which exhibit hardening and embrittlement due to precipitation induced by high-energy neutron irradiation. According to previous publications [5–7], the source of this equation goes back to a paper published in 1958 [17]. This information appears to be incorrect; Eq. (1) is not mentioned in it. For future reference, here we provide the detailed derivation method of Eq. (1) as follows.

When a gliding dislocation is pinned by a precipitate particle (**Figure 5**), the force acting on the dislocation (F) is given as a function of bowing angle (θ) and the line tension (T):

$$F = 2T\cos(\theta/2) \tag{2}$$

The force acting on a dislocation line is alternatively given as a function of a shear stress (τ), the Burgers vector (b), and the length of dislocation line, which is in this case the distance between particles (L):

$$F = \tau bL \rightarrow \tau = \frac{2T}{bL}\cos(\theta/2) \tag{3}$$

By adopting the simplest approximation for the line tension of dislocations, i.e., $T = \mu b^2/2$, we obtain:

$$\tau = \frac{\mu b}{L}\cos(\theta/2)(\rightarrow = \alpha\mu b/L) \tag{4}$$

The obstacle strength (α) corresponds to the bowing angle (θ). In the case where the precipitate particle is an impenetrable obstacle, the dislocation eventually bypasses the obstacle with forming a dislocation loop around it (**Figure 4**). The formation of dislocation loop occurs at θ = 0°, where the segments of dislocation line on both sides of the obstacle become parallel from each other. Those segments have the same Burgers vector and opposite line senses, thereby they are attracted each other and eventually merged into one. At θ = 0°, F becomes a maximum value (=2 T). In other words, the maximum value of α is 1. Degree of precipitation hardening in macroscopic length scale is denoted by the tensile stress rather than the shear stress; they converted each other using the Taylor factor ($\tau = \sigma/M$):

$$\Delta\sigma_y = \frac{M\mu b}{L}\cos(\theta/2)(\rightarrow = \alpha M\mu b/L) \tag{5}$$

Eq. (5) is converted into Eq. (1), based on the simplest approximation for the spatial distribution of precipitates, i.e., a square lattice arrangement:

$$L = 1/N_s^{1/2} = 1/(2rN_v)^{1/2} = 1/(N_v d)^{1/2} \tag{6}$$

where N_s is the number of precipitate particles per unit area on a plane (i.e., the planar number density) and r is the mean radius of precipitates. The relation of $N_s = 2rN_v$ is derived from the Delesse's principle [18], where the volume fraction of precipitate particles in 3D space (V_V) is equivalent to their area fraction in 2D space (A_A):

$$V_V = A_A$$

$$N_v \times \left(\frac{4\pi r^3}{3}\right) = N_s \times \pi(r')^2$$

$$N_v \times \left(\frac{4\pi r^3}{3}\right) = N_s \times \pi\left(\frac{r}{1.22}\right)^2$$

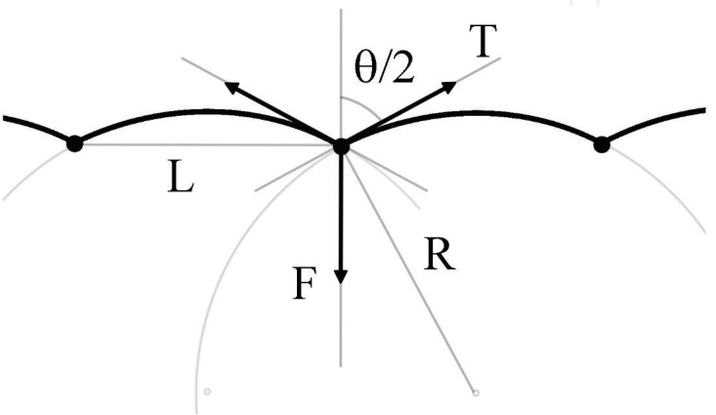


Figure 5.
Dislocation on a slip plane where each obstacle exerts localized glide resistance force (F) balanced in equilibrium by line tension forces (T).

$$N_s \approx 2rN_v \tag{7}$$

The average radius of particles measured on 2D space (r') is a function of their true radius (r): r' = r/1.22. This relationship is derived as follows [19]. The radius (r') varies with the position of sectioning plane relative to the center of sphere:

$$r' = \sqrt{r^2 - h^2} \tag{8}$$

where h is the distance from the center to the sectioning plane. The probability that the test plane intersects the sphere at a distance between h and h + Δh from its center is dh/r. The average of the area of section $\overline{\pi(r')^2}$ is obtained by applying the definition of mean value [19] as follows:

$$\overline{\pi(r')^2} = \int_0^r \pi\left(r^2 - h^2\right)\frac{dh}{r} = \frac{2}{3}\pi r^2$$

$$(r')^2 = \frac{2}{3}r^2$$

$$r \approx 1.2247r' \tag{9}$$

The obstacle strength α is 1 for particles dispersed in an ideal square lattice arrangement but ~0.8 for those dispersed randomly. This is an empirical rule obtained from 2D simulations performed by Foreman and Makin (**Figure 6**). The motion of dislocations is not uniform, but they propagate preferentially through "local soft spots" where the local number density of obstacles is smaller than the others (**Figure 7**). As a result of such spatially localized deformation, the average stress level required to sweep a unit area becomes smaller than the case of square arrangement.

An alternative explanation of $\alpha \neq 1$ is obtained from a geometry analysis (**Figure 8**) considering the possibility that effective average interparticle distance (Λ) on the slip plane may be different from the actual average interparticle distance (L) in 3D space due to the effect of a dislocation-obstacle interaction on another interaction. This concept is based on an assumption that the lattice friction against dislocation glide is negligibly small, in a steady-state plastic deformation at a

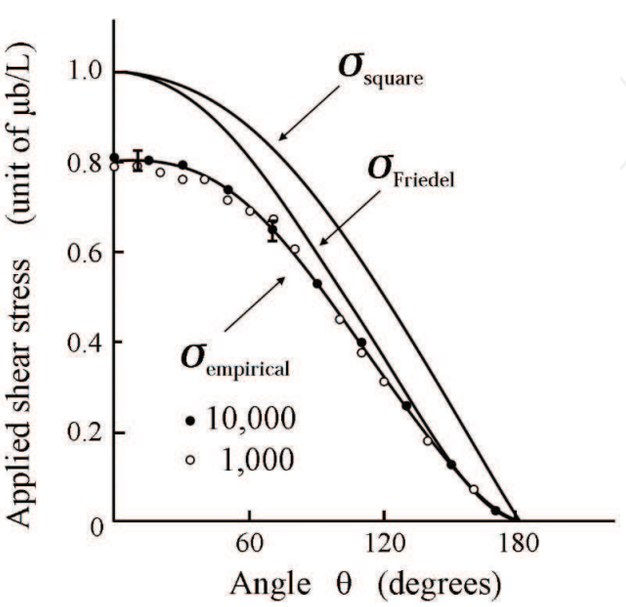


Figure 6.
Simulation results of Foreman and Makin [12] in comparison with the Orowan model, which assumes a square lattice arrangement of obstacles, and a calibrated model based on the Friedel's assumption shown in ***Figure 14****.*

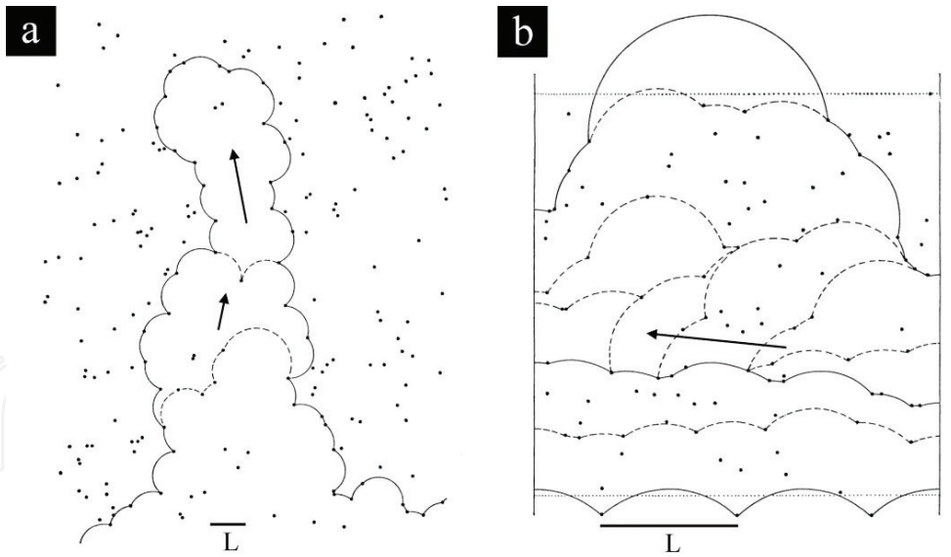


Figure 7.
Simulation results of Foreman and Makin [12]: (a) strong obstacles and (b) weak obstacles. The arrows indicate the propagation direction of dislocations.

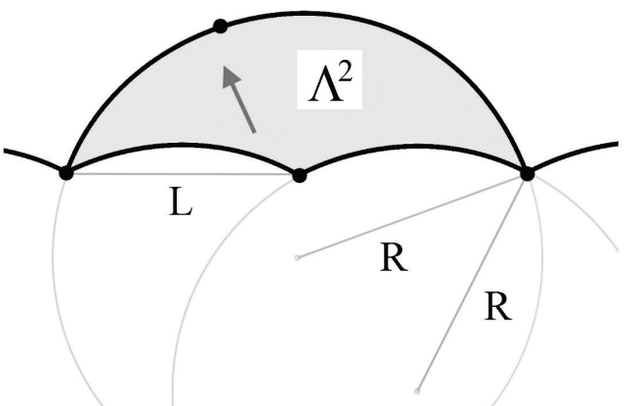


Figure 8.
A geometry consideration of simultaneous interaction of a dislocation with multiple obstacles. When a dislocation segment starts interacting with an obstacle, this segment is already curved due to the aftereffect of previous interaction with another obstacle. Since the dislocation segment sweeps an area between obstacles without any additional stress (when the friction is assumed to be negligibly small), the average flow stress becomes smaller that of the case of single obstacle interaction (and also the square lattice arrangement). Consequently, their effective obstacle strength becomes smaller.

constant strain rate. In this case, after unpinning from an obstacle, the curvature of a dislocation remains unchanged until it encounters another obstacle [20] (**Figure 8**). If the area swept by such motion of dislocations upon unpinning is greater than the area occupied by one obstacle in the average of 3D space (given as a regular square lattice arrangement), it follows that the apparent stress level required to sweep a unit area becomes smaller. The area swept by the dislocation (Λ^2) is regarded as the effective area occupied by a single particle on the slip plane. This area is the area of large segment of a circle of radius (R) minus that of two small ones:

$$\Lambda^2 = \left[\mathrm{R}^2 \sin^{-1}\left(\frac{L}{2R}\right) - \frac{L}{4}\sqrt{4R^2 - L^2}\right] - 2\left[\mathrm{R}^2 \sin^{-1}\left(\frac{L}{R}\right) - L\sqrt{R^2 - L^2}\right] \quad (10)$$

This formula cannot be solved unless otherwise some kind of approximation is introduced. A common approximation of L < <R results in $\Lambda^2 = 0$. Judging from the geometry shown in **Figure 8**, a rather approximation is L = R.

$$\Lambda^2 = \left(\frac{\pi}{6} + \frac{\sqrt{3}}{2}\right) L^2$$
$$\Lambda \approx 1.18L \tag{11}$$

In this case, a factor of 1/1.18 = 0.85 is introduced into Eq. (4). In other words, the maximum value of α is 0.85 if this geometry effect is considered. It is noteworthy that this value coincides with the coefficient of the well-known Ashby-Orowan model [16]. The Ashby-Orowan model adopted this value from Kocks' works, which consist of a graphical analysis performed on 550 obstacles in random distribution [13] and a geometry consideration expressed in a more complicated form than this analysis [15].

Eq. (1) is, although obtained from simplified assumptions in terms of the line tension of dislocations and the spatial distribution of precipitates, helpful for intuitive understanding about the effects of precipitate size and number density on hardening. Using this formula, here we evaluate the magnitude of hardening as a function of those factors in fcc Cu, bcc Fe, hcp Ti, and hcp Mg. Under a constant volume fraction of precipitates, smaller size results in greater hardening due to:

$$V_v = N_v \times \left(\frac{4\pi r^3}{3}\right) \tag{12}$$

Smaller size results in higher number density. In many cases, the maximum value of the number density of precipitates introduced by thermal aging is $\sim 1 \times 10^{23} m^{-3}$, which corresponds to an interparticle distance of ~22 nm in the case of the square lattice distribution. With this number density, when the volume fraction is 2%, it follows that the diameter of particles is 7.3 nm (**Table 1**). In the case of bcc Fe, the yield strength is estimated to be ~1.4 GPa, ~10 times greater than the yield strength without precipitates, ~120 MPa. Irradiation with high-energy particles such as neutron often induces (or enhance) precipitation of second phase. The number density of irradiation-induced precipitates can become the order of $10^{24}/m^3$, which corresponds to an interparticle distance of 10 nm. For instance, the number density and diameter of neutron irradiation-induced Cu precipitates and Ni—Si—Mn precipitates are both some $10^{24}/m^3$ and 0.5–1.5 nm, respectively [21]. Their volume fractions are 0.007% for 0.5 nm and 0.18% for 1.5 nm. Their hardening is estimated to be 1.1 GPa for the former and 1.9 GPa for the latter. For reference, the magnitude of hardening in the bcc Fe, the fcc Cu, the hcp Ti, and the hcp Mg as a function of volume fractions and diameter of precipitates is summarized in **Figures 1** and **2**.

Number density [m^{-3}]	Volume fraction [%]	Diameter [nm]	Interparticle distance [nm]	Δσ [MPa]
2×10^{23}	2	5.8	17.1	1750
1×10^{23}	2	7.3	21.5	1365
1×10^{22}	2	15.6	46.4	631
1×10^{21}	2	34	100	295
1×10^{20}	2	73	215	137

Table 1.
Estimation of realistically achievable maximum precipitation hardening in bcc iron at a constant volume fraction (2%) with variation of number density and mean diameter of precipitate particles.

3. Effects of crystallography on obstacle strength

After Orowan, extensive studies have been made on the effects of various factors such as dislocation character (edge vs. screw), spatial distribution of precipitates and their size distribution, elastic anisotropy, stacking fault energy, coherency, formation of ledges at the precipitate/matrix interface due to passage of dislocations (a.k.a. chemical strengthening), formation of antiphase boundary at the interface (a.k.a. ordering strengthening), etc. However, the effect of crystallography of precipitates has long been unexplored until very recently, partly due to technical difficulties in experiments. The absence of simulations on this issue is due to the following two reasons. (1) For molecular dynamics (MD) simulations, reproducing the realistic interaction geometry between gliding dislocations and incoherent particles is technically rather difficult, because experimental databases on the atomic structures of the precipitate-matrix interphases are limited. (2) For dislocation dynamics (DD) simulations based on continuum elasticity theory calculations, the effect of crystal mismatch is beyond the capability.

In 2016 it was experimentally demonstrated that soft precipitates can be strong obstacles. That report examined bcc Nb precipitates in hcp Zr matrix, the shear modulus of which are 28 and 33 GPa, respectively. Traditionally, the obstacle strength of such soft precipitates has been scaled by the difference of the shear modulus between precipitates and matrix in accordance with a model proposed by Russell and Brown in 1972 [22]. An implication of the Russell-Brown model is that a greater difference in the shear modulus results in a greater obstacle strength, as described later. Since the Nb precipitates in the Zr—2.5Nb alloy are as soft as the Zr matrix, they are considered weak obstacles. Nevertheless, their experimentally determined obstacle strength was α = 0.8–1 (**Figure 9**), indicating that they are ideal Orowan-type strong obstacles. This analysis result is supported by transmission electron microscopy (TEM) observation (**Figure 10**). The morphology of the Nb precipitates does not change even after severe cold rolling up to 90%; they are certainly non-shearable obstacles. Later, Matsukawa et al. further demonstrated that, by means of transmission Kikuchi diffraction (TKD), crystal orientation of the Nb precipitates is practically random (as described in the previous section of this chapter). Considering that dislocations can glide only on specific atomic planes, the most probable scenario is probably that dislocations cannot cut through the

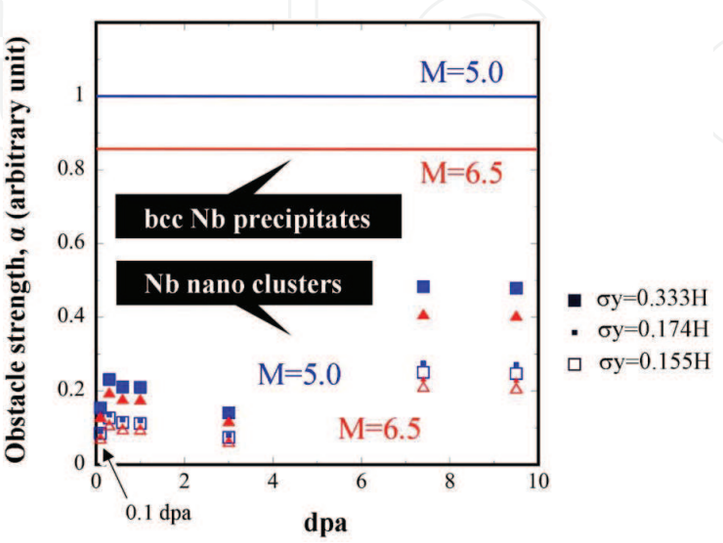


Figure 9.
Experimentally determined obstacle strength of bcc Nb precipitates and irradiation-induced Nb nanoclusters in Zr—Nb alloys [3]. The former was obtained from Zr—Nb alloys containing various amounts of bcc Nb precipitates, whereas the latter from a Zr—2.5Nb alloy subjected to ion irradiation.

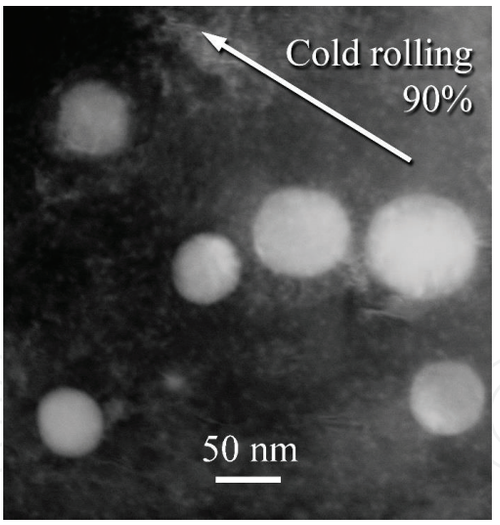


Figure 10.
Bcc Nb precipitates in a Zr—2.5Nb alloy subjected to cold rolling up to 90% [4]. Although the bcc Nb is softer than the hcp Zr in terms of shear modulus, the bcc Nb precipitates in the hcp Zr matrix are actually nonshearable, strong obstacles against gliding dislocations.

precipitates as the slip plane of precipitate interior is not parallel to the slip plane of the matrix.

The hcp Zr matrix of the Zr—2.5Nb alloy contained Nb ~0.5 at.%, which is greater than the solubility (see **Figure 10** of the previous chapter). The excess Nb atoms formed nanoprecipitates when the alloy is subjected to high-energy particle irradiation. Unlike the bcc Nb precipitates whose α is 0.8–1, the α of the Nb nanoprecipitates produced by irradiation was estimated to be ~0.2 or less. Their obstacle strength α is plotted in **Figure 9** as a function of damage level (displacement per atom: dpa). This analysis is based on an assumption that the irradiation-induced hardening occurred solely due to nanoprecipitates. In reality, however, the irradiated samples may also have contained defect clusters such as dislocation loops at high density. This assumption yields an overestimation of the α of nanoprecipitates; nevertheless, the obtained α was extremely small, indicating that the Nb nanoclusters are weak obstacles. The origin of such small α of nanoprecipitates is presumably attributable to the structural change of precipitates

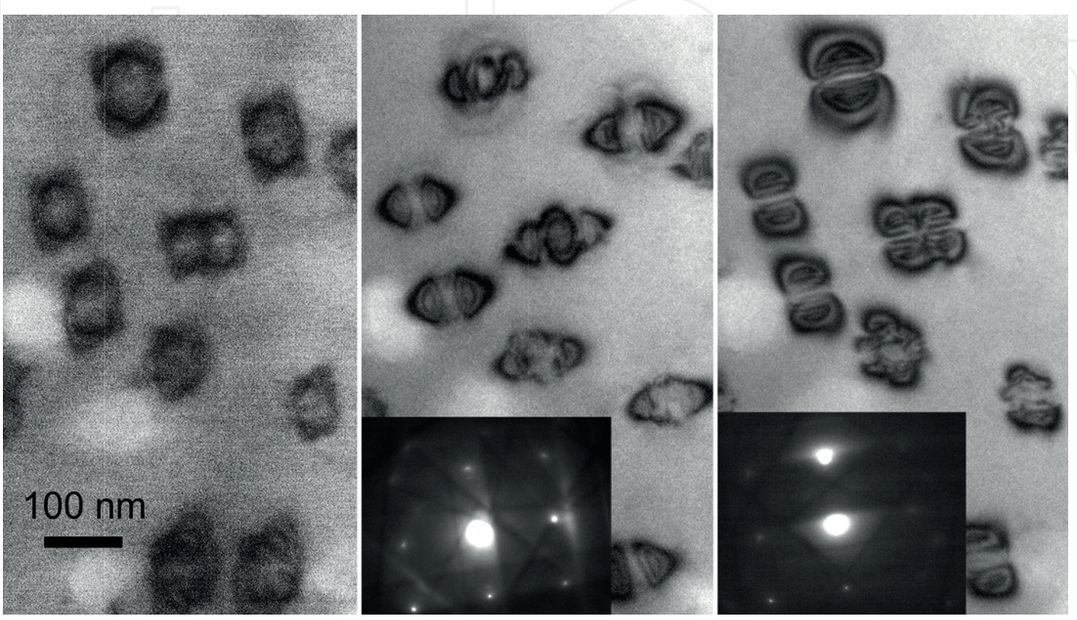


Figure 11.
Coherent fcc Co precipitates embedded in fcc Cu matrix of a Cu-3 wt.% Co alloy [23]. The strain contrast around the precipitate particles in undeformed samples is lost in deformed samples.

during precipitation described in the previous chapter. This hypothesis is still open for further investigation.

Soft precipitates can become non-shearable obstacles against dislocations due to the effect of crystallography. Likewise, hard precipitates can become shearable if crystallography allows, i.e., when their slip plane is parallel to that of the matrix. An example shown here is a coherent fcc Co precipitate particle embedded in fcc Cu matrix [23] (**Figure 11**). The shear modulus of the fcc Co is about two times greater than that of the fcc Cu [24]; nevertheless, the Co precipitates are actually shearable (**Figure 12**). It still remains unclear how much hard particles are shearable. It appears that this process occurs only in a limited circumstance. The Co particles were sheared only when interacted with Shockley partial dislocations having the same Burgers vector, gliding on adjacent {111} planes, forming a twin band. Otherwise, dislocations bypassed the Co precipitates via the Hirsch mechanism [25] (**Figure 13**). The Hirsch mechanism is similar to the Orowan mechanism but distinct in terms of the type of dislocation loop remained after the interaction.

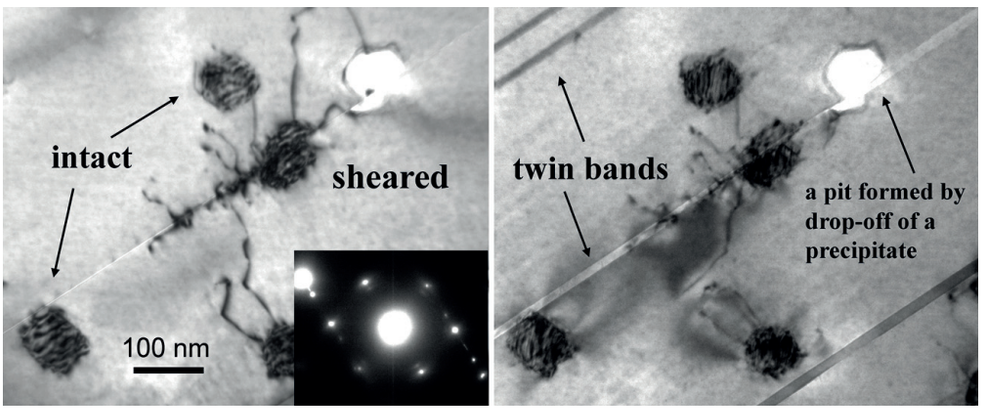


Figure 12.
Cutting of strong obstacles by dislocations: fcc Co precipitates in fcc Cu matrix [25]. The shear modulus of the fcc Co is two times larger than the fcc Cu [24].

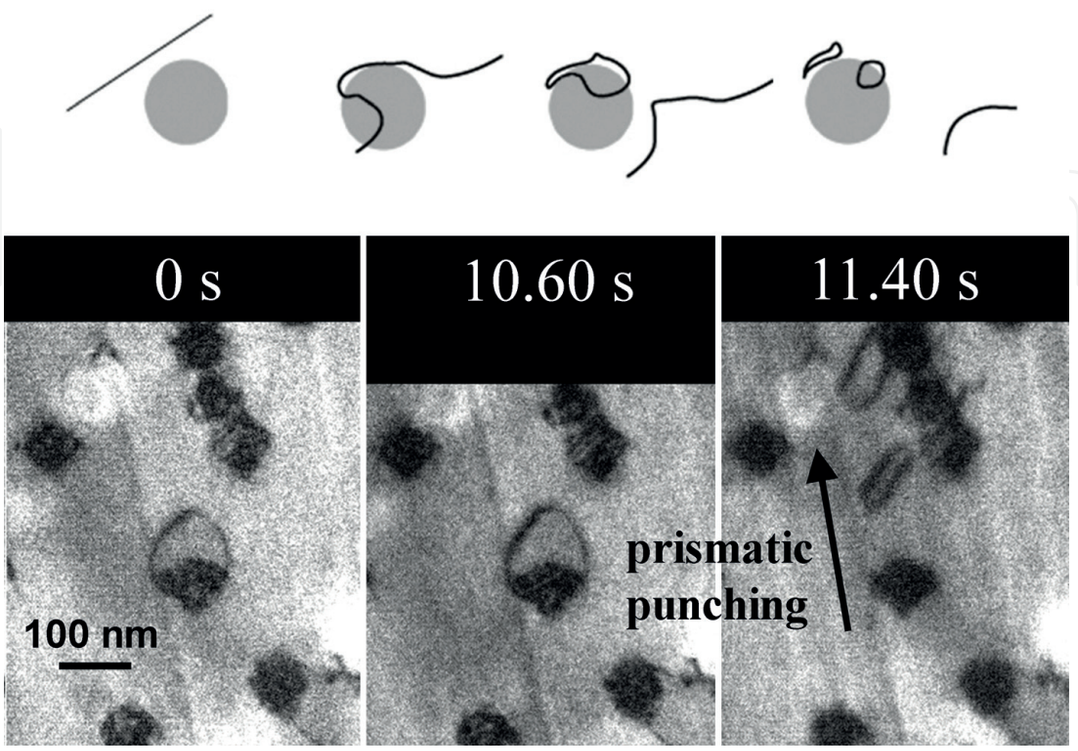


Figure 13.
The Hirsch mechanism [26] observed by TEM in situ straining experiments: fcc Co precipitates in fcc Cu matrix [25].

The Orowan loop is a shear dislocation loop whose Burgers vector is parallel to the loop plane, whereas the Hirsch mechanism produces a prismatic loop [26] whose Burgers vector is not parallel. When the Burgers vector is perpendicular to the loop plane, the prismatic often exhibit one-dimensional back and forth motion along the Burgers vector [27]. The Hirsch mechanism is frequently observed in TEM in situ straining experiments using thin foil specimens, which have a less constraint for deformation in the thickness direction (i.e., so-called plane stress condition). In such a thin foil geometry, screw dislocations that compensate the out-of-plane shear displacements are dominant over edge dislocations [28]. Screw dislocations exhibit cross slip (slip transfer from the slip plane to another slip plane) on non-shearable obstacles. The Hirsch mechanism is induced by the cross slip of screw dislocations on the surface of obstacles [25]. Hence, the Hirsch mechanism is probably dominant over the Orowan mechanism in the deformation of thin foil samples.

4. Precipitation hardening due to solute clusters

Precipitation hardening is a key research subject not only for developing new, strong materials but also for estimating the engineering lifetime of existing materials. For instance, engineering lifetime of reactor pressure vessels (RPVs) of light-water nuclear reactors is determined by embrittlement due to precipitation of minor alloying elements such as Cu, Ni, Mn, and Si rather than accumulation of irradiation damages. Since the RPVs are practically non-replaceable due to economic reasons, their engineering lifetime determines the useful lifetime of entire power plants. Establishing a predictive model of material embrittlement (loss of ductility) is a long-standing challenge in fundamental physical metallurgy. Although the theory of dislocations is well established for quantitatively describing the strength of materials, the dislocation theory is incapable of directly describing the ductility. Hence, the loss of ductility has often been indirectly scaled by the degree of hardening, based on a generally accepted empirical rule that stronger materials exhibit less ductility. The size of irradiation-induced precipitates in the RPV steels is typically a few nm. In the early stage of precipitation, they may be solute clusters rather than second-phase particles crystallographically distinct from the matrix.

In order to evaluate hardening due to solute clusters, the Orowan model needs a modification as follows. The simulation by Foreman and Makin was performed not only on strong obstacles but also on weak obstacles. In **Figure 6** empirical results of their simulations are plotted as a function of bowing angles (θ), together with outputs of two theoretical models: one is the Orowan model with a square lattice arrangement, and the other is a model obtained based on Friedel's geometry consideration (a.k.a the Friedel's statistics) [29, 30] similar to **Figure 8**. In the Friedel's concept the angle (β) of **Figure 14** is assumed to be very small, i.e., $L << R$, which is a realistic approximation for weak obstacles. In fact, the simulation results were in good agreement with this model at bowing angles of greater than ~100°. The formula based on the Friedel's approximation is obtained as follows [29, 30]:

$$F = 2T\sin\beta = \tau b(2\beta R) \rightarrow 2T\beta \approx 2\tau b\beta R \rightarrow R = \frac{T}{\tau b} \tag{13}$$

$$\sin\beta = \frac{L}{R} \rightarrow \beta \approx \frac{L}{R} \tag{14}$$

$$\tan\left(\frac{\beta}{2}\right) \approx \frac{h}{L} \rightarrow \frac{\beta}{2} \approx \frac{h}{L} \rightarrow h = \frac{L^2}{2R} \tag{15}$$

$$\Lambda^2 \approx Lh \tag{16}$$

From Eqs. (13) and (15), (16), we obtain.

$$\Lambda^2 = \frac{L^3}{2R} = \frac{\tau b L^3}{2T} \rightarrow \mathrm{L} = \left(\frac{2T\Lambda^2}{\tau b}\right)^{1/3} = \left(\frac{\mu b \Lambda^2}{\tau}\right)^{1/3} \tag{17}$$

From Eqs. (4) and (17), the following relationship is obtained [12]:

$$L = \frac{\mu b}{\tau}\cos(\theta/2) = \left(\frac{\mu b \Lambda^2}{\tau}\right)^{1/3}$$

$$\left(\frac{\mu b}{\tau}\right)^3 [\cos(\theta/2)]^3 = \frac{\mu b \Lambda^2}{\tau}$$

$$\tau^2 = \left(\frac{\mu b}{\Lambda}\right)^2 [\cos(\theta/2)]^3$$

$$\tau = \frac{\mu b}{\Lambda}[\cos(\theta/2)]^{3/2} \tag{18}$$

By replacing Λ with L, this formula is generalized as follows [12]:

$$\tau = \frac{\mu b}{\mathrm{L}}[\cos(\theta/2)]^{3/2} \quad \theta \geq 100^{\circ} \tag{19}$$

In practice, however, applying Eq. (19) to the analysis of weak obstacles is not straightforward; it is difficult to evaluate how much weak the obstacles are. The Russell-Brown model [22] is an alternative model, more practically useful than the previous model for this purpose (**Figure 15**). This model was originally developed for Cu precipitates in Fe—Cu steels; the crystal structure of which is not fcc but bcc in the early stage of precipitation. In this model the obstacle strength is scaled by the ratio of the energy of dislocation segments in precipitates and in matrix. The energy of dislocations is dependent on the shear modulus. The shear modulus of fcc Cu is lower than bcc Fe. According to the results of ab initio calculations, the shear modulus of bcc Cu is even smaller. The energy of dislocation segment inside the Cu precipitate is lower than that in the matrix Fe.

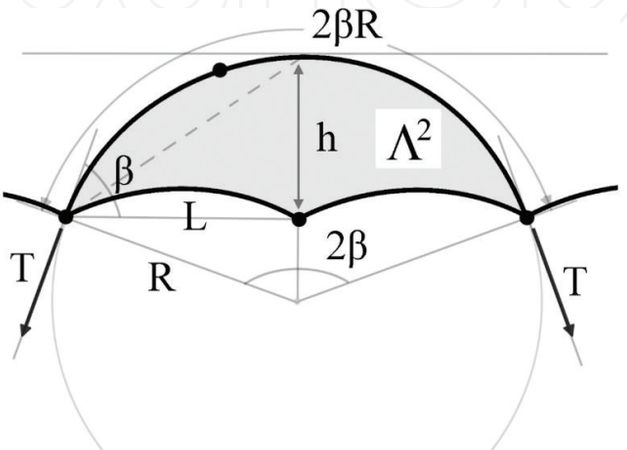


Figure 14.
Friedel's geometry consideration of dislocation-obstacle interactions [29, 30]. This approximation assumes L < <R, i.e., 2β 0, whereas the other previously discussed in ***Figure 8*** *assumes L = R.*

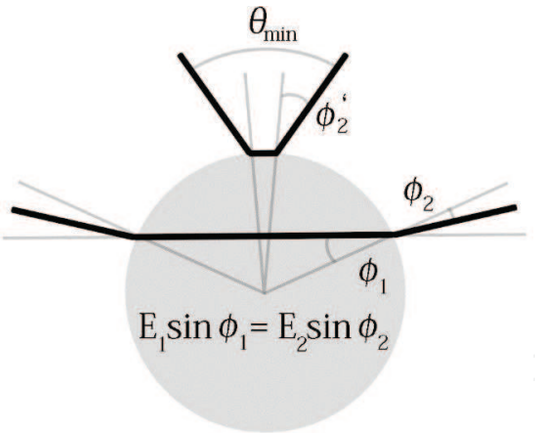


Figure 15.
The Russell-Brown model for weak obstacles [23]. This model scales the obstacle strength of soft precipitates by the ratio of shear modulus between precipitates and matrix.

In accordance with the aforementioned empirical knowledge obtained from the simulation of Foreman and Makin, on the applicability limit of the Orowan model in terms of dislocation bowing angle, when $\sin^{-1}(E_1/E_2) \leq 50°$,

$$\tau = 0.8\frac{\mu b}{L}\left[1-\left(\frac{E_1}{E_2}\right)^2\right]^{1/2}, \sigma = 0.8\frac{M\mu b}{L}\left[1-\left(\frac{E_1}{E_2}\right)^2\right]^{1/2}. \quad (20)$$

When $\sin^{-1}(E_1/E_2) \geq 50°$,

$$\tau = \frac{\mu b}{L}\left[1-\left(\frac{E_1}{E_2}\right)^2\right]^{3/4}, \sigma = \frac{M\mu b}{L}\left[1-\left(\frac{E_1}{E_2}\right)^2\right]^{3/4} \quad (21)$$

The energy ratio is given as follows:

$$\frac{E_1}{E_2} = \frac{E_1^{\infty}\log\frac{r}{r_0}}{E_2^{\infty}\log\frac{R}{r_0}} + \frac{\log\frac{R}{r}}{\log\frac{R}{r_0}} \quad (22)$$

where E_1^{∞} and E_2^{∞} refer to the energy per unit length of a dislocation in infinite media, r is the radius of precipitates, and r_0 and R are the inner and outer cutoff radius (they adopted $R = 10^3 r_0$). Since the energy of dislocation is proportional to the shear modulus, the ratio of energy $E_1^{\infty}/E_2^{\infty}$ is equal to the ratio of shear modulus G_1/G_2 for a screw dislocation, and $\frac{G_1(1-\nu_2)}{G_2(1-\nu_1)}$ for an edge dislocation (ν: the Poisson's ratio)—in the case of bcc Cu precipitates embedded in bcc Fe matrix, 0.59 for the former and 0.64 for the latter.

The Russell-Brown model indicates that, even in the case where precipitates are softer than the matrix, they become weak obstacles only when their shear modulus is slightly smaller than the matrix. Two extreme conditions, $E_1^{\infty} = E_2^{\infty}$ and $E_1^{\infty} = 0$, correspond to the situations of "no obstacle" and "the strongest obstacle," respectively. The latter may be consistent with our empirical knowledge that voids are the strongest obstacles, obtained from experiments [31] and from MD simulations [32, 33]. Although the Russell-Brown model indicates that those which are as soft as the matrix are weak obstacles, as mentioned earlier, such precipitates can also become ideal Orowan-type strong obstacles if the slip plane inside the precipitates is not parallel to that of the matrix [3–4]. From this respect, the situation where precipitate particles become weak obstacles against dislocations may be rather rare. The Russell-Brown model has been applied to the analysis of irradiation-induced

hardening of RPV steels due to not only Cu precipitates but also Ni—Si—Mn precipitates [34–37], though it remains unclear whether the Ni—Si—Mn precipitates are softer than the matrix. If they were harder than the matrix ($E_1^{\infty} > E_2^{\infty}$), it may not be mathematically valid to apply the Russell-Brown model to them, regardless of whether they are shearable obstacles. Furthermore, the effect of crystal structure change during precipitation has not been considered thus far.

Acknowledgements

The author was supported by the MEXT Grant-in-Aid for Young Scientists (A) (22686058), by Japan Society for the Promotion of Science (JSPS) KAKENHI (#16K06767) and by The Iron & Steel Institute of Japan (ISIJ) the 23rd and the 26th Research Promotion Grants. This review article is based on the author's previous researches partly sponsored by the Ministry of Education, Culture, Sports, Science and Technology (MEXT) of Japan, under the Strategic Promotion Program for Basic Nuclear Researches entitled "Study on hydrogenation and radiation effects in advanced nuclear fuel cladding materials" and "Study of degradation mechanism of stainless steel weld-overlay cladding of nuclear reactor pressure vessels" and a program entitled "R&D of nuclear fuel cladding materials and their environmental degradations for the development of safety standards" entrusted to Tohoku University by the MEXT. Those researches were also supported in part by the Collaborative Research Programs of "the Oarai Center" and "the Cooperative Research & Development Center for Advanced Materials" of the Institute for Materials Research, Tohoku University, and of the Research Institute for Applied Mechanics, Kyushu University; by Advanced Characterization Nanotechnology Platform, Nanotechnology Platform Program of the MEXT, Japan at the Research Center for Ultra-High Voltage Electron Microscopy in Osaka University and at the Ultramicroscopy Research Center in Kyushu University; and by the Joint Usage/Research Program on Zero-Emission Energy Research, Institute of Advanced Energy, Kyoto University (ZE27C-07, ZE28C-09, ZE29C-11, and ZE30C-01).

Conflict of interest

The author declares no conflicts of interest directly relevant to the content of this article.

IntechOpen

IntechOpen

Author details

Yoshitaka Matsukawa[1,2]

1 Faculty of Advanced Science and Technology, Division of Materials Science, Kumamoto University, Kumamoto, Japan

2 Institute for Materials Research, Tohoku University, Sendai, Miyagi, Japan

*Address all correspondence to: ym2@msre.kumamoto-u.ac.jp

IntechOpen

© 2019 The Author(s). Licensee IntechOpen. This chapter is distributed under the terms of the Creative Commons Attribution License (http://creativecommons.org/licenses/by/3.0), which permits unrestricted use, distribution, and reproduction in any medium, provided the original work is properly cited. CC BY

References

[1] Orowan E. Discussion. In: Symposium on Internal Stresses in Metals and Alloys, Institute of Metals; Monograph and Report Series 5. London: Institute of Metals; 1948. pp. 451-453

[2] Ardell AJ. Precipitation hardening. Materials Transactions. 1985;**16A**: 2131-2165

[3] Matsukawa Y, Yang HL, Saito K, Murakami Y, Maruyama T, Iwai T, et al. The effect of crystallographic mismatch on the obstacle strength of second phase precipitate particles in dispersion strengthening: bcc Nb particles and nanometric Nb clusters embedded in hcp Zr. Acta Materialia. 2016;**102**: 323-332

[4] Matsukawa Y, Okuma I, Muta H, Shinohara Y, Suzue R, Yang HL, et al. Crystallographic analysis on atomic-plane parallelisms between bcc precipitates and hcp matrix in recrystallized Zr–2.5Nb alloys. Acta Materialia. 2017;**126**:86-101

[5] Rice RM, Zinkle SJ. Temperature dependence of the radiation damage microstructure in V ± 4Cr ± 4Ti neutron irradiated to low dose. Journal of Nuclear Materials. 1998;**258–263**: 1414-1419

[6] Zinkle SJ, Matsukawa Y. Observation and analysis of defect cluster production and interactions with dislocations. Journal of Nuclear Materials. 2004; **329–333**:88-96

[7] Hashimoto N, Byun TS, Farrell K, Zinkle SJ. Deformation microstructure of neutron-irradiated pure polycrystalline metals. Journal of Nuclear Materials. 2004;**329–333**: 947-952

[8] Armstrong RW. 60 years of Hall-Petch: Past to present nano-scale connections. Materials Transactions. 2014;**55**:2-12

[9] Shen JH, Li YL, Wei Q. Statistic derivation of Taylor factors for polycrystalline metals with application to pure magnesium. Materials Science and Engineering A. 2013;**582**:270-275

[10] Leguey T, Baluc N, Schäublin R, Victoria M. Structure-mechanics relationships in proton irradiated pure titanium. Journal of Nuclear Materials. 2002;**307–311**:696-700

[11] Conrad H. The rate controlling mechanism during yielding and flow of titanium at temperatures below 0.4 T_m. Acta Metallurgica. 1966;**14**:1631-1633

[12] Foreman AJE, Makin MJ. Dislocation movement through random arrays of obstacles. Philosophical Magazine. 1966;**15**:911-924

[13] Kocks UF. A statistical theory of flow stress and work hardening. Philosophical Magazine. 1966;**13**: 541-546

[14] Kocks UF. On the spacing of dispersed obstacles. Acta Metallurgica. 1966;**14**:1629-1631

[15] Kocks UF. Statistical treatment of penetrable obstacles. Canadian Journal of Physics. 1967;**45**:737-755

[16] Ashby MF. The theory of the critical shear stress and work hardening of dispersion-hardened crystals. In: Ansell GS et al., editors. Oxide Dispersion Strengthening. New York: Gordon and Breach; 1968. pp. 143-205

[17] Seeger AK. 2nd UN Conference on Peaceful Uses of Atomic Energy. Vol. 6. United Nations, New York; 1958. p. 250

[18] Delesse A. Ueber die mineralogische und chemische Beschaffenheit der

Gesteine der Vogesen. Journal für Praktische Chemie. 1948;**43**:417-448

[19] DeHoff RT, Rhines FN. Quantitative Microscopy. New York: McGraw-Hill; 1968. pp. 21-23, 139-140

[20] Bacon DJ, Osetsky YN, Rodney D. Dislocation-obstacle interactions at the atomic level. In: Hirth JP, Kubin L, editors. Dislocations in Solids. Amsterdam: Elsevier; 2009. pp. 75, 85-136, 228-237

[21] Integrity of Reactor Pressure Vessels in Nuclear Power Plants. Assessment of Irradiation Embrittlement Effects in Reactor Pressure-Vessel Steels. IAEA Nuclear Energy Series No. NP-T-3.11. Vienna: International Atomic Energy Agency; 2009. pp. 63-63

[22] Russell KC, Brown LM. A dispersion strengthening model based on differing elastic moduli applied to the iron-copper system. Acta Metallurgica. 1972;**20**: 969-974

[23] Matsukawa Y, Liu GS. In-situ TEM study on elastic interaction between a prismatic loop and a gliding dislocation. Journal of Nuclear Materials. 2012;**425**: 54-59

[24] Shim J-H, Voigt H-JL, Wirth BD. Temperature dependent dislocation bypass mechanism for coherent precipitates in Cu-Co alloys. Acta Materialia. 2016;**110**:276-282

[25] Matsukawa Y. Unpublished data

[26] Hatano T. Dynamics of a dislocation bypassing an impenetrable precipitate: The Hirsch mechanism revisited. Physical Review B. 2006;**74**:020102(R)

[27] Matsukawa Y, Zinkle SJ. One-dimensional fast migration of vacancy clusters in metals. Science. 2007;**318**: 959-962

[28] Matsukawa Y, Osetsky YN, Stoller RE, Zinkle SJ. Mechanisms of stacking fault tetrahedra destruction by gliding dislocations in quenched gold. Philosophical Magazine. 2008;**88**: 581-597

[29] Friedel J. Dislocations. Oxford: Paragon Press; 1964. pp. 220-228, 371-382

[30] Friedel J. On the elastic limit of crystals. In: Electron Microscopy and Strength of Crystals. Proc. 1st Barkeley Int'l Mater. Conf. New York: Interscience Publishers (A Division of John Wiley & Sons); 1963. pp. 605-649

[31] Lucas GE. The evolution of mechanical property change in irradiated austenitic stainless steels. Journal of Nuclear Materials. 1993;**206**: 287-305

[32] Bacon DJ, Osetsky YN, Rodney D. Dislocation-obstacle interactions at the atomic level. In: Hirth JP, Kubin L, editors. Dislocations in Solids. Vol. 15. Amsterdam: Elsevier; 2009. pp. 1-160

[33] Hatano T, Matsui H. Molecular dynamics investigation of dislocation pinning by a nanovoid in copper. Physical Review B. 2005;**72**:094105

[34] Takeuchi T, Kuramoto A, Kameda J, Toyama T, Nagai Y, Hasegawa M, et al. Effects of chemical composition and dose on microstructure evolution and hardening of neutron-irradiated reactor pressure vessel steels. Journal of Nuclear Materials. 2010;**402**:93-101

[35] Kuramoto A, Toyama T, Takeuchi T, Nagai a Y, Hasegawa M, Yoshiie T, et al. Post-irradiation annealing behavior of microstructure and hardening of a reactor pressure vessel steel studied by positron annihilation and atom probe tomography. Journal of Nuclear Materials. 2012;**425**:65-70

[36] Kuramoto A, Toyama T, Nagai Y, Inoue K, Nozawa Y, Hasegawa M, et al. Microstructural changes in a Russian-type reactor weld material after neutron irradiation, post-irradiation annealing and re-irradiation studied by atom probe tomography and positron annihilation spectroscopy. Acta Materialia. 2013;**61**:5236-5246

[37] Shimodaira M, Toyama T, Yoshida K, Inoue K, Ebisawa N, Tomura K, et al. Contribution of irradiation-induced defects to hardening of a low copper reactor pressure vessel steel. Acta Materialia. 2018;**155**:402-409